Materials Horizons

Freeze
on
heating

ROYAL SOCIETY
OF CHEMISTRY

COMMUNICATION
Eric Collet *et al.*
Stabilizing low symmetry-based functions of materials
at room temperature through isosymmetric electronic
bistability

COMMUNICATION

Stabilizing low symmetry-based functions of materials at room temperature through isosymmetric electronic bistability†

Francisco Javier Valverde-Muñoz, [ID] [a] Ricardo Guillermo Torres Ramírez, [ID] [a] Elzbieta Trzop, [ID] [ab] Thierry Bataille, [ID] [c] Nathalie Daro, [d] Dominique Denux, [d] Philippe Guionneau, [ID] [d] Hervé Cailleau, [a] Guillaume Chastanet, [d] Boris Le Guennic [ID] [c] and Eric Collet [ID] *[abe]

Symmetry-breaking is pivotal for controlling ferroelectric, ferroelastic and/or ferromagnetic functions of materials, which enables applications in sensors, memory devices, transducers or actuators. Commonly, ferroic phases emerge from descending symmetry-breaking, as the laws of thermodynamics dictate that the ordered low entropy phases form at low temperature, which limits practical applications of many materials at room temperature. Rare examples of ascending symmetry-breakings have been observed, but the driving force remains often unclear. Here, we report on a ferroelastic symmetry-breaking occurring at high temperature in a spin-crossover material, studied by magnetic, DSC and X-ray diffraction measurements. Our DFT calculations and our model, based on the Landau theory of phase transitions, explain how the cooperative thermal switching of the molecular spin state drives a ferroelastic symmetry breaking at high temperature, through a coupled Jahn–Teller distortion. Ferroelastic materials have rich properties, with important applications in memory, multifunctional and novel controllable devices. The electronic bistability in soft functional materials represents an important source of entropy gain, capable of overcoming the cost of symmetry-breaking entropy, which opens up new perspectives for stabilizing high-temperature and low-symmetry ferroic functions of advanced materials.

New concepts

In this manuscript, we present the concept of generating symmetry-breaking based functions of materials at high temperature, which is made possible by coupled electronic instability. Symmetry breaking is responsible for the emergence of functions associated with different types of ferroic orders, enabling applications in sensors, memory devices, transducers or actuators. However, symmetry breaking usually occurs during cooling, as phases with low symmetry are often those with low entropy. This fact severely limits the practical applications of many materials at room temperature. This study highlights the effectiveness of using an electronic bistability, corresponding here to spin-crossover, as a large source of entropy gain upon warming to overcome the entropy cost of a coupled symmetry breaking, corresponding here to a ferroelastic distortion. The importance of the coupling between both types of instabilities has been proven through a combination of magnetic, calorimetric and structural experiments and theoretical models. This communication thus demonstrates a proof-of-concept of ascending symmetry-breaking driven through an isosymmetric electronic instability, which opens up the way to applications for functionalized materials operating at high temperature and more particularly at room temperature.

1. Introduction

The study of solid-state phase transitions lies at the very heart of materials science.[1] The associated changes in physical properties and functions, which can be driven by many external control parameters such as temperature, pressure, magnetic or electric field, and even light, give rise to various types of applications for materials. In a large class of phase transitions, materials exhibit a symmetry-breaking,[2,3] where the associated ordering of structural and/or electronic degrees of freedom is responsible for the emergence of various functions related to ferromagnetism, ferroelectricity, ferroelasticity, multiferroicity,

[a] Univ Rennes, CNRS, IPR (Institut de Physique de Rennes) – UMR 6251, 35000 Rennes, France. E-mail: eric.collet@univ-rennes.fr

[b] CNRS, Univ Rennes, DYNACOM (Dynamical Control of Materials Laboratory) – IRL 2015, The University of Tokyo, 7-3-1 Hongo, Tokyo 113-0033, Japan

[c] Univ Rennes, Ecole Nationale Supérieure de Chimie de Rennes, CNRS, ISCR (Institut des Sciences Chimiques de Rennes) – UMR 6226, F-35000 Rennes, France

[d] Univ. Bordeaux, CNRS, Bordeaux INP, ICMCB, UMR 5026, F-33600 Pessac, France

[e] Institut Universitaire de France (IUF), France

or conductivity.[4–12] According to thermodynamics, in the general situation of symmetry-breaking (SB), the high temperature (HT) phase always has higher entropy and higher symmetry than the low-symmetry and low temperature (LT) phase. These types of SB processes have been rationalized in the framework of the Landau theory of phase transitions,[2,3] where the LT phase results from the loss of some symmetry operators of the HT phase.

The degree of SB below a critical temperature T_{SB} is characterized by the order parameter η. In the simplest case, when η is scalar and continuous symmetry breaking occurs, the SB Gibbs energy is expanded in a series of even powers of η:

$$G_{SB}(T,\eta) = \frac{a_0}{2}(T - T_{SB})\eta^2 + \frac{b}{4}\eta^4 \qquad (1)$$

The stability conditions $\left(b > 0, \frac{dG_{SB}}{d\eta} = 0, \frac{d^2 G_{SB}}{d\eta^2} > 0\right)$ are balanced by the η^2 coefficient. For $a_0 > 0$, the high-symmetry phase ($\eta = 0$) is stable above T_{SB}. Below T_{SB}, the low-symmetry phase is characterized by two symmetry-equivalent solutions $\pm\eta = \sqrt{\frac{a_0}{b}(T_{SB} - T)}$, with $G_{SB}(T) = -\frac{1}{4b}[a_0(T_{SB} - T)]^2$ and the SB entropy $S_{SB} = -\frac{\partial G_{SB}}{\partial T} = \frac{a_0^2}{2b}(T - T_{SB})$. Fig. 1a illustrates this usual descending symmetry-breaking, stabilizing the low-symmetry phase below T_{SB}, as rationalized through the $\eta(T)$ and $S_{SB}(T)$ curves. In this way, the symmetry of a material and its entropy commonly increase upon warming, as η decreases and the high-symmetry phase is the high entropy one.

Recently, a counter idea emerged:[13,14] can the symmetry of a material decrease with increasing temperature? This situation corresponds to $a_0 < 0$ (Fig. 1c), which means that the SB entropy decreases above T_{SB}. Another source of entropy gain is then required to comply with thermodynamics. Thus, few systems exhibit such unusual and counter-intuitive ascending symmetry-breakings. A famous example is ^{3}He, which exhibits a liquid-to-solid phase transition upon warming.[15] It is due to the larger entropy in the solid state, originating from disordered nuclear spins, compared to the quantum Fermi nature of the liquid state. Other ascending symmetry-breakings have attracted sustained interest in superconducting,[16] ferroelectrics[17] or magnetic[18] materials. These are often associated with re-entrant phase transitions, where the low-symmetry phase is intermediate between two high-symmetry LT and HT phases and forms over a narrow temperature range due to competing interactions or frustrations.[16,18–20] However, the origin of the increasing entropy, required to stabilize the low-symmetry phase at high temperature, is often difficult to identify. Here, we report on an ascending ferroelastic symmetry-breaking in a molecular spin crossover (SC) material, which cannot be understood by considering only the associated change of symmetry. Our study sheds a new light on the entropy stabilization process.

SC materials[21–24] exhibit more or less cooperative thermal conversions of their molecular electronic state from low-spin (LS) to high-spin (HS). This is monitored at the macroscopic scale through the totally symmetric SC parameter $q = \frac{N_{HS} - N_{LS}}{N_{HS} + N_{LS}}$, where N_{LS} and N_{HS} refer to the number of molecules in each state. The spin crossover phenomenon is isosymmetric, i.e. it occurs without change of symmetry, like gas–liquid transitions. SC occurring around T_{SC} is described in the simplest way[25,26] through the spin crossover Gibbs energy:

$$G_{SC}(T,q) = a_1(T_{SC} - T)q + \frac{B}{2}q^2 + \frac{C}{4}q^4 \qquad (2)$$
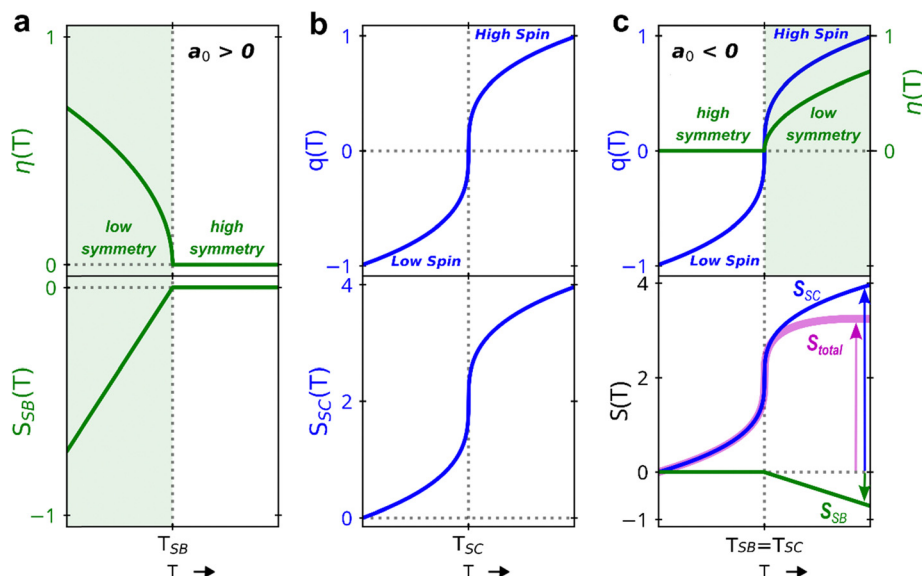
Fig. 1 Basics of Landau theory. (a) Usual descending symmetry-breaking (SB, $a_0 > 0$). The low-symmetry phase (green area) forms below T_{SB}, characterized by SB parameter $\eta(T)$ and SB entropy (S_{SB}). (b) Spin crossover (SC) curve $q(T)$ driven by the entropy increase (S_{SC}) in the high spin state. (c) Concept of ascending symmetry-breaking ($a_0 < 0$) upon heating: the SB entropy cost S_{SB} can be largely compensated by the SC entropy gain S_{SC}. The total entropy, $S_{tot} = S_{SB} + S_{SC}$, increases then upon warming, stabilizing a high spin and low symmetry phase at high temperature.

The first term accounts for the coupling of q to the conjugated field. When elastic interactions are strong ($B < 0$) LS and HS phases coexist around T_{SC}, while a crossover regime appears for $B > 0$. For the intermediate critical regime ($B = 0$), T_{SC} corresponds to the critical temperature. Then, the stability conditions of eqn (2) $\left(a_1 > 0, C > 0, \dfrac{dG}{dq} = 0, \dfrac{d^2G}{dq^2} > 0\right)$ give obvious analytical solutions:

$$q = \left[\frac{a_1}{c}(T - T_{SC})\right]^{\frac{1}{3}} \text{ and } G_{SC} = -\frac{3}{4}\left[\frac{[a_1(T_{SC} - T)]^4}{C}\right]^{\frac{1}{3}}.$$

The $q(T)$ plot in Fig. 1b shows the SC phenomenon around T_{SC}, which is also an entropy-driven process.[21,22] Indeed, the SC entropy increases from LS to HS states, with

$$S_{SC} = a_1\left[\frac{a_1(T - T_{SC})}{C}\right]^{\frac{1}{3}}.$$

In several SC materials, spin crossover and symmetry-breaking phenomena compete.[25–27] In these SC materials, the coupling of the isosymmetric SC electronic bistability to the SB allows for controlling symmetry-related functions, such as conductivity, magnetic order, multiferroicity or giant magneto-electric response, through spin state conversion upon thermal, optical or magnetic stimuli.[27–33]

In particular, ferroelastic materials have rich properties, with important applications in memory, multifunctional and novel controllable devices.[4,8–10] However, the ferroelastic phases usually form at low temperature, which limits further applications. Here we present and discuss the unusual emergence of an ascending symmetry-breaking in the high temperature phase of the SC material $[Fe^{II}(PM\text{-}PEA)_2(NCS)_2]$. It exhibits a low-spin high-symmetry phase (LShs) at low temperature and a ferroelastic high-spin low-symmetry phase (HSls), stable above 235 K. Our crystallographic and magnetic measurements highlight the coupling between SC and SB phenomena. DFT calculations reveal a Jahn–Teller instability in the high-spin state, breaking molecular symmetry. Our Landau model, describing the effect of the coupling between the two clearly identified SC and SB instabilities, rationalizes the emergence of a low-symmetry high temperature phase. Fig. 1c schematically shows the concept, where the entropy cost due to symmetry-breaking at high temperature is largely compensated by the entropy gain due to spin crossover.

2. Materials and methods

2.1. Synthetic procedures

Our measurements were performed on black needle-shaped single crystals, obtained in methanol after a few days by slow diffusion of the iron solution through a methanol layer into the ligand solution, in a straight tube under an inert atmosphere. More details can be found in previous work.[34]

2.2. Magnetic measurements

We collected data at 5 K min^{-1} from one single crystal glued with cryogenic GE7031 varnish to a 3 mm wide 15 cm long 0.725 mm thick strip cut out of a 200 mm high purity CZ type Si wafer whose diamagnetic contribution has been previously recorded.

2.3. X-ray diffraction

X-ray diffraction measurements of the $[Fe^{II}(PM\text{-}PEA)_2(NCS)_2]$ molecular material were performed as a function of temperature on a single crystal from 80 to 300 K and powder from 300 to 520 K. Complete experimental details can be found in the Sections S1–S4 in the ESI.†

2.4. DSC measurements

Differential scanning calorimetry measurements were performed in the 115–295 K temperature range under argon on a PerkinElmer calorimeter DSC8000 coupled with a CLN2 regulator setting a scan rate of 5 K min^{-1} on 8.034 mg of crystals (Section S7 in the ESI†).

2.5. Computational details

DFT geometry optimizations were carried out by using the Gaussian 16 (revision A.03) package[35] with the PBE0 hybrid functional[36,37] and tightening both self-consistent field (10^{-10} a.u.) and geometry optimization (10^{-5} a.u.) convergence thresholds (Section S5 in the ESI†).

3. Results and discussion

3.1. Spin crossover

The $[Fe^{II}(PM\text{-}PEA)_2(NCS)_2]$ compound exhibits a spin-transition with a thermal hysteresis loop.[34] Fig. 2a shows the temperature dependence of its $\chi_M T$ product, where χ_M is the molar magnetic susceptibility and T is the temperature. $\chi_M T$ directly relates to the SC parameter q (right axis), through the weighted contribution of the number N_{HS} of paramagnetic HS sites (χ_M^{HS} with $S = 2$) and N_{LS} of diamagnetic LS sites (χ_M^{LS} with $S = 0$). In the HT phase, $\chi_M^{HS} T \simeq 3.5$ cm^3 K mol^{-1}, which corresponds to a fully HS state ($q = 1$). As temperature is lowered, q drops around $T_\downarrow \simeq 219$ K in the LT diamagnetic phase and gradually reaches a fully LS macroscopic state below 150 K. The characteristic $\chi_M T$ value close to 0 corresponds to $q = -1$. In contrast to polycrystalline powder samples,[34,38] single-crystals exhibit a 16 K wide thermal hysteresis, with a clear single-step conversion upon cooling and two different conversion regimes upon heating: the gradual one from 150 K to $T_\uparrow \simeq 235$ K, followed by a discontinuous jump towards the HS state. It was shown recently that contrary to isosymmetric SC, with symmetric conversion curves around T_{SC} (Fig. 1b), such unsymmetric hysteresis loops are characteristic of the coupling between symmetry-breaking and spin crossover.[25]
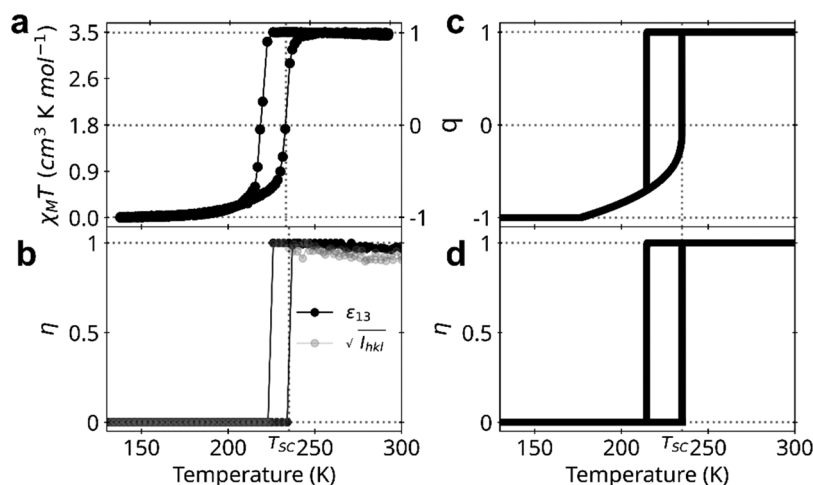
Fig. 2 Coupled spin transition and ferroelastic distortion. (a) Thermal dependence of the spin transition order parameter $q(T)$, monitored through $\chi_M T = \left[\left(\frac{1+q}{2} \right) \chi_M^{HS} + \left(\frac{1-q}{2} \right) \chi_M^{LS} \right] \times T$. (b) Thermal dependence of the symmetry-breaking parameter $\eta(T)$ measured through the ferroelastic distortion $|\varepsilon_{13}|$ and the intensity of symmetry-breaking Bragg peaks $(\eta \propto \sqrt{I_{hkl}})$, both normalized to unity for clarity. All measurements are performed on a single crystal. (c) and (d) Corresponding thermal dependence of SB and SC parameters obtained from our Landau model based on eqn (4).
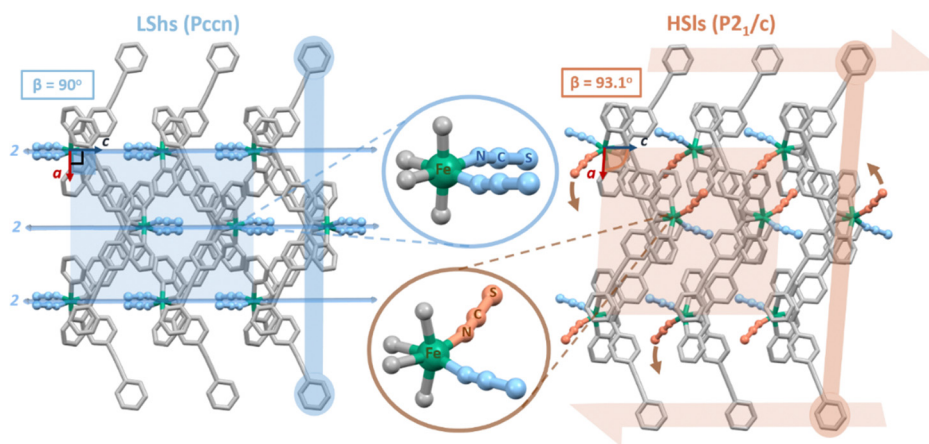
3.2. Ferroelastic symmetry-breaking at high temperature

From previous reports on $[Fe^{II}(PM\text{-}PEA)_2(NCS)_2]$,[34] it was unclear whether the change between orthorhombic LS and monoclinic HS space groups corresponded to a reconstructive process[39] or to a group–subgroup symmetry-breaking.[3] However, this is a key point for its analysis in the framework of Landau theory, which only accounts for the latter case.[2] To learn more about the structural reorganization, we collected X-ray diffraction data on a single crystal upon cooling and heating, to monitor the changes in lattice parameters and Bragg peak intensities (Section S3, ESI†). The ferroelastic phase transition, characterized by the deviation of the lattice β angle from 90° to 93.1°, corresponds to a symmetry-breaking with a group–sub-group relationship between the $Pccn$ space group of the parent-paraelastic LShs and the $P2_1/c$ space

group of the daughter-ferroelastic HSls phase (Fig. 3).[40–42] This long-range ferroelastic distortion is monitored through the amplitude of the symmetry-breaking spontaneous strain:[4,40,42] $|\varepsilon_{13}(T)| = \left| \frac{1}{2} \left(\frac{c(T)\cos(\beta(T))}{c_0(T)} \right) \right|$. In principle, a continuous $Pccn \leftrightarrow P2_1/c$ phase transition line can exist. However, Fig. 2 shows that $|\varepsilon_{13}(T)| \propto \eta(T)$, referred to as the symmetry-breaking order parameter hereafter, changes discontinuously at $T_\downarrow \simeq 221$ K and $T_\uparrow \simeq 235$ K (Fig. 2b). $\eta(T) = 0$ in the LShs phase and $\eta(T)$ is almost constant in the HSls phase from 221 to 300 K. The analysis of powder diffraction patterns indicates that the daughter and high temperature ferroelastic HSls phase, characterized by the splitting of (hkl) and $(\bar{h}kl)$ Bragg peaks, remains stable up to $\simeq 500$ K, beyond which the sample melts (Fig. S5, ESI†). This ascending SB from LT to HT phases is also

Fig. 3 Symmetry-breaking ferroelastic transition. Change of crystalline symmetry from the LT parent-paraelastic LShs $Pccn$ phase to the HT daughter-ferroelastic HSls $P2_1/c$ phase. The 2-fold molecular axes (2) along c in the LShs state are lost in the HSls phase, which is associated with a shear of the molecular layers (orange arrows) opening the β angle, and an asymmetric torsion of the PM-PEA ligands and thiocyanate groups (NCS zoom).

characterized by the change of Bragg peak extinction rules (Section S4, ESI†). The intensities I_{hkl} of the $(0kl)$ Bragg peaks with $l = 2n + 1$ and $(hk0)$ Bragg peaks with $h + k = 2n + 1$ are zero in the Pccn LShs phase and non-zero in the $P2_1/c$ HSls phase. Fig. 2b shows the thermal dependence of $\sqrt{I_{hkl}(T)} \propto \eta(T)$ for these symmetry-breaking Bragg peaks, confirming the discontinuous symmetry change between the LT LShs and the HT HSls phases. The lattice parameters (Fig. S3, ESI†) also exhibit discontinuous changes upon heating and cooling during the phase transition, resulting in a large volume strain $v_s \simeq 0.05$ in the HSls phase. These data evidence the concomitant evolutions of the spin transition parameter q through the volume strain v_s, the lattice parameters, the intensity of symmetry-breaking Bragg peaks, and the ferroelastic distortion ε_{13} from the Pccn LS LT phase to the $P2_1/c$ HS HT phase. These results characterize the coupling between SC and SB phenomena, which exhibit the same thermal hysteresis between LShs and HSls phases. This coupling between both phenomena is known to be driven by long-range elastic interactions.[25] The slight broadening of thermal hysteresis in magnetic data (measured at 5 K min^{-1}) compared to quasi-static XRD data is known to be due to kinetic effects.

Fig. 3 shows the crystalline structure of [Fe^{II}(PM-PEA)$_2$(NCS)$_2$] along the b axis of the lattice in the fully LS (90 K) and HS (300 K) states. The crystal packing exhibits a ferroelastic distortion, corresponding to a shear of the molecular layers in the HSls phase. The resulting deviation of the lattice angle β from 90° to 93.1° is related to the loss of the $C2$ symmetry. In the Pccn LShs space group, the molecules are located on Wyckoff positions with $C2$ symmetry along the c molecular axis, while in the $P2_1/c$ HSls phase, the $C2$ symmetry is lost, with distorted molecules in general positions. This is characterized by an important torsion of the thiocyanate groups and a moderate rearrangement of the PM-PEA ligands in the HSls state, initially equivalent in the LShs state. The intra-molecular structural parameters,[43] such as the ⟨Fe–N⟩ bond lengths and N–Fe–N torsion angles, are characteristic of LS and HS states (Section S2, ESI†). Fig. S6 (ESI†) shows that the monoclinic HSls state can also be quenched by flash cooling at 30 K, while the evolution of v_s and ε_{13} indicates that the relaxation towards the orthorhombic LShs ground phase occurs around 65 K upon heating. These results underline the strong coupling between the molecular spin state (q) and the crystalline and molecular symmetries (η).

Then comes the chicken-egg question: is the spin crossover responsible for symmetry-breaking, or *vice versa*?

3.3. DFT analysis of the Jahn–Teller distortion in the high spin state

For understanding the coupled molecular changes of spin state and symmetry, we performed DFT calculations on the isolated molecule (Section S5, ESI†). In the LS state, we optimized the molecular structure with $C2$ point symmetry of the Wyckoff position of the molecular sites in the LShs lattice.

The results provide positive frequencies for all the 231 intramolecular vibrational modes with A or B symmetry. This indicates that the molecular structure in the LShs state is stable with respect to the $C2$ symmetry, with symmetry-equivalent thiocyanate groups and PM-PEA ligands (Fig. 4). The energy diagram of the molecular orbitals in the LShs and HShs states with C2 symmetry shows the degeneracy of some orbitals with symmetric thiocyanate groups. In contrast, the structure of the HShs state with $C2$ symmetry is unstable, as characterized by the negative frequency of one torsion mode Q_T (B symmetry, Fig. S9 and Video S1, ESI†).

The molecular torsion along Q_T stabilises the HS state, as schematically shown in Fig. 4, which lowers molecular symmetry towards $C1$. The optimized molecular structure in the HSls state with $C1$ symmetry is stable (all modes have positive frequencies), and the structural distortion of the thiocyanate groups correlates with their asymmetric spin density in the HSls state. The overall molecular distortion in the HSls state provided by DFT calculations is in good agreement with crystallographic data. These calculations reveal the microscopic origin of the symmetry-breaking, due to the Jahn–Teller distortion along Q_T in the HSls state, characterized by an asymmetric bending of the Fe^{2+}–(NCS$^-$)$_2$ dipoles as the 2-fold molecular axis is lost.

Our DFT results underline again the strong coupling between the spin state and symmetry, as the Jahn–Teller distortion stabilizes the high-spin state.

### 3.4. Coupled symmetry-breaking and spin crossover

Describing the LShs to HSls phase transition requires considering the contributions of both the SB (eqn (1)) and SC (eqn (2)) phenomena to the Landau thermodynamical potential as well as their coupling terms. This approach was used for other materials[25,44] to describe their phase diagrams and explain why SC and SB phenomena can occur sequentially or simultaneously. Hereafter we use the symmetry-relevant potential:

$$G(q, \eta) = a_1(T_{SC} - T)q + \frac{B}{2}q^2 + \frac{C}{4}q^4 + \frac{a_0}{2}(T - T_c)\eta^2 + \frac{b}{4}\eta^4 + Dq\eta^2 + \frac{E}{2}q^2\eta^2 \tag{3}$$

The couplings ($D < 0$ and $E < 0$) contribute to stabilizing the LShs ($q = -1$, $\eta = 0$) and the HSls ($q = 1$, $\eta \neq 0$) phases revealed by experiments and DFT calculations. It should be underlined that, compared to other studies related to "improper" linear-quadratic coupling considered in the literature,[39,45] here it is the inclusion of the symmetry-allowed q term that balances the relative stability of HS and LS states through their entropy difference. It was shown that this phenomenological coupling includes both the elastic energy and elastic coupling of both parameters to lattice strains, which is responsible for cooperative elastically driven phase transitions.[25,44] In order to further simplify the model, we consider the intermediate critical crossover case ($B = 0$), and we use the strong coupling limit (Section S6, ESI†), for which $\frac{a_0}{2}(T - T_c) \ll Dq$. Then the potential
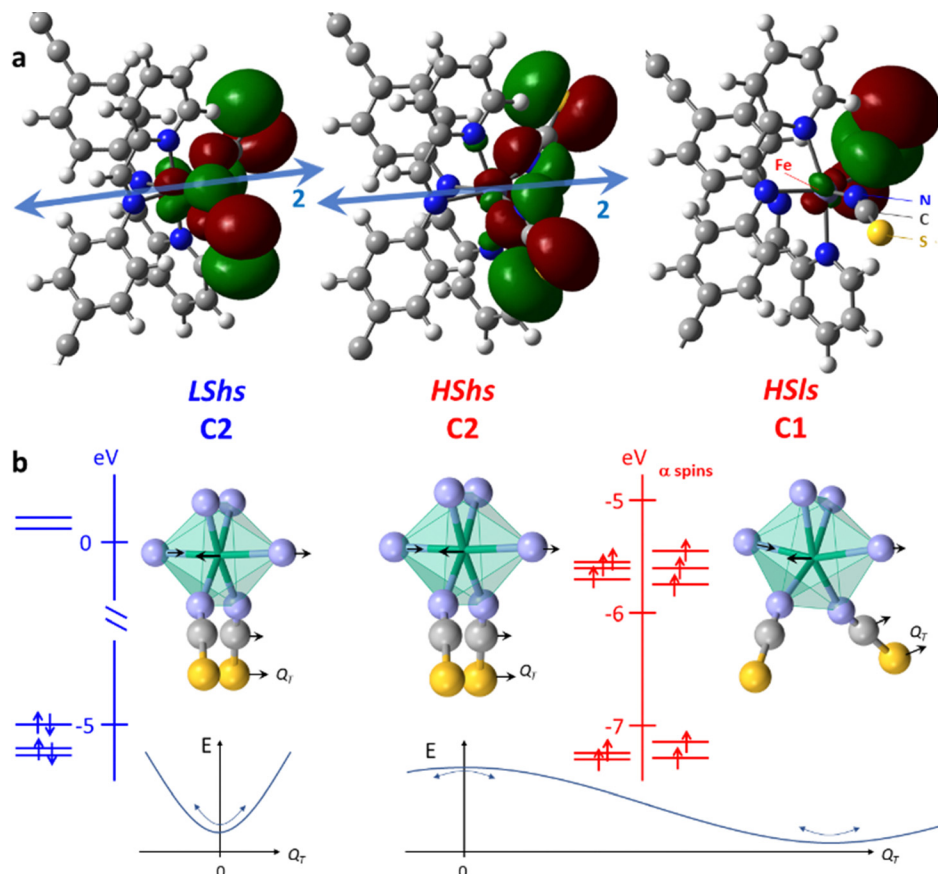
Fig. 4 Comprehensive summary of DFT calculations. (a) Optimized molecular structure for $C2$ LShs, $C2$ HShs and $C1$ HSls states. The loss of the 2-fold molecular axis in the HSls state with the molecular torsion results in asymmetric orbitals, especially around the NCS groups. (b) Zoomed in image of the FeN$_4$(NCS)$_2$ core, with energy diagram of t_{2g}-like and e_g-like orbitals showing the splitting of orbital degeneracy from $C2$ (LShs and HShs) to $C1$ (HSls), where only α spins are shown for clarity. The $C2$ HShs state is unstable along one torsion mode Q_T (B symmetry), which has a negative frequency. The main atomic motions for Q_T (see ESI,† Video S1) are schematically represented by arrows for the atoms surrounding the Fe. This Jahn–Teller distortion breaks $C2$ symmetry and brings the molecule towards the stable HSls state with $C1$ symmetry.

reduces to:

$$G(q, \eta) = a_1(T_{SC} - T)q + \frac{C}{4}q^4 + \frac{b}{4}\eta^4 + Dq\eta^2 + \frac{E}{2}q^2\eta^2 \quad (4)$$

The equilibrium (q, η) values are found by minimizing the Gibbs energy in eqn (4). $\eta = 0$ is stable for $q < 0$, which corresponds to the LShs phase. For $q > 0$, the two symmetry-equivalent stable solutions, $\left(\pm\eta = \sqrt{-(2Dq + Eq^2)/b}\right)$, correspond to the two possible ferroelastic domains in the HSls phase upon the $Pccn \rightarrow P2_1/c$ symmetry breaking.[40–42] Fig. 5 shows how the equilibrium (q, η) values change with temperature, considering the spin transition parameter as explicitly restricted to $-1 \leq q \leq 1$. Fig. 2c and d show the $q(T)$ and $\eta(T)$ curves calculated from eqn (4). These are in very good agreement with the experimental data, as they reproduce the main experimental features of the phase transition. (i) On heating from the fully LShs state ($q = -1$, $\eta = 0$) a SC starts as q gradually increases (Fig. 2a and c). (ii) Above the critical temperature $T_\uparrow$, the LShs phase is no more stable and a discontinuous transition occurs towards the HSls phase, where $q > 0$ is stabilized by

the SB ($\eta \neq 0$). (iii) The couplings maximize q to 1, which corresponds to the fully HS state. The amplitude of the SB parameter is then constant $\left((\eta = \sqrt{-(2D + E)/b})\right)$ in the HSls phase (Fig. 2b and d). (vi) The coupling terms generate an energy barrier in the potential, which stabilizes the HSls (G_{HL}, Fig. 5) and precludes gradual conversion towards LS on cooling. The HSls state is then stable down to $T_\downarrow$, where the LShs phase is reached. The potential in eqn (4) differs therefore in the low-symmetry ($\eta \neq 0$) and high-symmetry ($\eta = 0$) phases and the coupling opens a thermal hysteresis for both q and η.

This cooperative and hysteretic phase transition is mediated by the elastic interactions within the lattice. The emergence of a ferroelastic ordering in the high temperature phase of a SC material, from 235 K to 500 K beyond which the material melts, offers new perspectives for ascending symmetry-breaking. Heat capacity measurements (Section S7 in ESI†) reveal large entropy changes between the HSls and LShs phases upon heating ($\Delta S = 62.8$ J mol^{-1} K^{-1}) and cooling ($\Delta S = 67.6$ J mol^{-1} K^{-1}). These values are within the usual 40–80 J mol^{-1} K^{-1} range for SC materials.[21] The entropy increase from LShs to HSls phases includes contributions from both SB
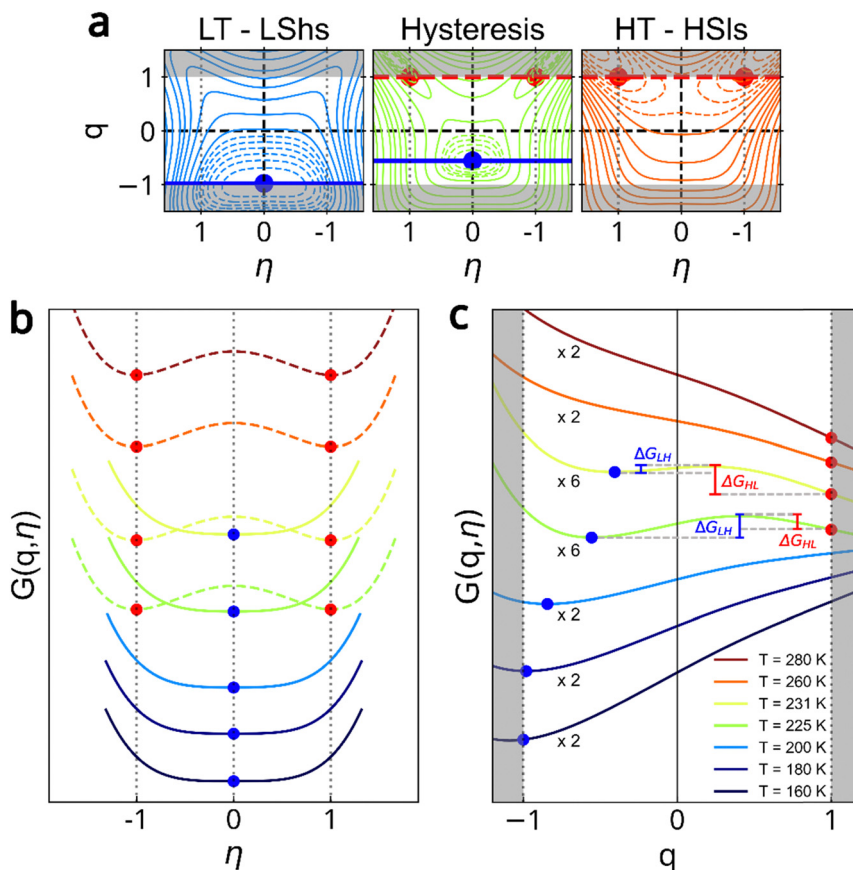
Fig. 5 Coupled spin crossover and symmetry-breaking. (a) Thermal dependence of the Gibbs energy $G(q, \eta)$ in the LT LShs phase ($q = -1$, $\eta = 0$ left), HT HSls phase ($q = -1$, $\eta \neq 0$ right) and inside hysteresis (middle) q is restricted to $-1 \leq q \leq 1$ (clear areas). (b) Cut of $G(q, \eta)$ along the SB order parameter (η) and SC order parameter (q) axes. q saturates to -1 at LT and gradually increases on approaching $T_\uparrow$, where it discontinuously jumps and saturates to 1 at HT. In the LShs phase $\eta = 0$, while in the HSls phase $\eta = \pm\sqrt{-(2D + E)/b}$, with $|\eta|$ normalized to 1 for clarity. The coupling stabilizes $q = 1$ on cooling down to $T_\downarrow$ as an energy barrier appears from LS to HS (G_{LH}) and HS to LS (G_{HL}) inside thermal hysteresis (curves are rescaled by 2 or 6 for a better visualization). The results are obtained from eqn (4) with $a_1 = 0.6$, $C = 35$, $b = 10$, $T_{SC} = 235$ K, $D = -6.5$, and $E = -12.2$.

and SC phenomena, which can be estimated based on theoretical calculations:

$$\Delta S_{theo} = \Delta S_{SB} + \Delta S_{SC}.$$

On the one hand, the symmetry-breaking entropy ΔS_{SB} is negative due to ascending symmetry-breaking. Indeed, if the ascending orthorhombic → monoclinic SB was purely order–disorder in character,[46] with molecules ordered on a single position in the HT phase and disordered between two positions equivalent by the $C2$ axis in the LT phase, the SB entropy would be $\Delta S_{SB} = R\ln(1) - R\ln(2) = -5.76$ J K^{-1} mol^{-1}. On the other hand, the SC phenomenon is a large source of entropy gain, responsible for the giant barocaloric effect,[21,47] with two main contributions: $\Delta S_{SC} = \Delta S_{spin} + \Delta S_{vib}$. ΔS_{spin} is due to different spin multiplicities ($\Omega = 2S + 1$) in HS ($S = 2$) and LS ($S = 0$) states: $\Delta S_{spin} = R(\ln(5) - \ln(1)) = 13.42$ J K^{-1} mol^{-1}. The vibrational entropy difference ΔS_{vib} is mainly due to the lower frequencies of the FeN$_6$ core vibrations in the less bonding HS state compared to LS.[21,22]

We estimated ΔS_{vib} for [Fe^{II}(PM-PEA)$_2$(NCS)$_2$] based on our DFT calculations of the frequencies of the vibrational modes in both spin states (Section S5, ESI†), which gives

$\Delta S_{vib} = 58.9$ J K^{-1} mol^{-1}. In this way, we calculate the theoretical entropy increase from LShs to HSls phases, which is clearly dominated by the vibrational entropy: $\Delta S_{theo} = \Delta S_{SB} + \Delta S_{spin} + \Delta S_{vib} = 66.5$ J K^{-1} mol^{-1}.

This calculated value is in nice agreement with our experimental value $\Delta S = 62.8 - 67.6$ J mol^{-1} K^{-1} obtained from calorimetric measurements (Fig. S12, ESI†). Thus, the molecular scale plays a central role in such materials, both for entropy stabilization, through numerous intra-molecular degrees of freedom, and for the Jahn–Teller distortion associated with the ferroelastic symmetry breaking.

Fig. 1c represents schematically this concept of ascending symmetry-breaking, where the SB entropy cost (ΔS_{SB}) can be largely compensated by the isosymmetric entropy gain (ΔS_{SC}) due to electronic bistability. However, a rigorous description of the concerted SC and SB phenomena requires considering the important role of their coupling, as explicitly discussed through our Landau model (Fig. 2 and 5). This coupling, which strongly stabilizes the HSls state, also plays a key role for the stabilization of HSls states trapped by flash cooling (Fig. S6, ESI†) or photoinduced.[48] Overall, the LShs → HSls ascending symmetry-breaking reported here corresponds to an

entropy-driven process, where the thermal SC starting upon warming drives the cooperative ferroelastic distortion above a critical conversion. This ascending symmetry breaking is the consequence of the collective distortions of the molecules in the lattice, due to cooperative elastic interactions. We can notice that a hypothetical parent para-elastic phase of high spin and high-symmetry ($Pccn$) could form around 800 K, as suggested by experimental data (see Fig. S5, ESI†), and our Landau model when the strong coupling limit vanishes (Fig. S11, ESI†). However, this HShs phase is not observed as the sample melts around 500 K.

4. Conclusions

Ascending symmetry-breaking is also observed in some spin crossover materials, as re-entrant phase transitions occur during stepwise spin transitions. In this case, a long-range HS–LS order appears on the step, due to competing elastic interactions. The intermediate half-conversion phase ($q = 0$), in between the high-symmetry LS and HS phases, exhibits symmetry-breaking ($\eta \neq 0$). It is stabilized by a bi-quadratic $q^2\eta^2$ coupling, but it forms only over a narrow temperature range[26,27,32,44,49] Instead, our study rationalizes how a symmetry-broken phase can be stabilized, through a coupled isosymmetric electronic bistability, over a broader and higher temperature range, here from 235 K and well above room temperature. Compared with hard-condensed matter, soft SC molecular materials exhibiting electronic bistability hold a large source of vibrational entropy gain. This substantial advantage opens up fascinating prospects for stabilizing robust low-symmetry phases in materials, enabling so the development of future generations of room-temperature ferroic devices, such as switches, force sensors and non-volatile memories.[4,50,51]

Regarding the ferroelastic domains forming after thermal cycling, it is well-established now that domain walls form 2D functional objects in their own right, which can be engineered to give rise to an electric polarization in an otherwise centrosymmetric system or to pyroelectric and electrocaloric effects in ferroelectric.[10,32,52] Regarding bulk properties, it was shown that an electric field can be used to substitute non-polar ferroelastic phases[53] exhibiting an antiferroelectric array of dipoles (such as the Fe^{2+}–$(NCS^-)_2$ bonds in Fig. 3), by a polar phase. The interesting thing about the single domain nature of the ferroelastic crystals $[Fe^{II}(PM\text{-}PEA)_2(NCS)_2]$, synthesized at room temperature, is that they can give rise to a single polar domain under the effect of an electric field.

The description of symmetry-breaking in the framework of the Landau theory of phase transitions is universal. Our model, considering a coupled electronic bistability successfully reproduced phase diagrams and the occurrence of simultaneous or sequential electronic bistability and SB phenomena in a broad variety of systems.[25,44] The present concept of ascending symmetry-breaking, where molecular positions get frozen during heating, coupled to an electronic instability can also apply

to ascending ferroelectricity or ferromagnetism, provided that the associated electrical or magnetic orders couple with an isosymmetric electronic bistability, acting as a source of significant entropy gain. These different types of ferroic orders result from different types of intermolecular interactions, which can be controlled through crystal engineering. This concept opens up the way to a rational design and applications for materials functionalized by their low symmetry and operating at high temperature.

Author contributions

Conflicts of interest

There are no conflicts to declare.

Acknowledgements

References

1 B. Fultz, *Phase Transitions in Materials*, Cambridge University Press, Cambridge, 2nd edn, 2020.
2 L. Landau, *Ukr. J. Phys.*, 2008, **53**, 25–35.
3 J. C. Tolédano and P. Tolédano, *The Landau Theory of Phase Transitions*, 1987.
4 E. K. H. Salje, *Annu. Rev. Mater. Res.*, 2012, **42**, 265–283.
5 G. Rogez, N. Viart and M. Drillon, *Angew. Chem., Int. Ed.*, 2010, **49**, 1921–1923.

6 T. Ishikawa, S. A. Hayes, S. Keskin, G. Corthey, M. Hada, K. Pichugin, A. Marx, J. Hirscht, K. Shionuma, K. Onda, Y. Okimoto, S. Y. Koshihara, T. Yamamoto, H. Cui, M. Nomura, Y. Oshima, M. A. Jawad, R. Kato and R. J. D. Miller, *Science*, 2015, **350**, 1501–1505.

7 S. Ohkoshi, K. Nakagawa, M. Yoshikiyo, A. Namai, K. Imoto, Y. Nagane, F. Jia, O. Stefanczyk, H. Tokoro, J. Wang, T. Sugahara, K. Chiba, K. Motodohi, K. Isogai, K. Nishioka, T. Momiki and R. Hatano, *Nat. Commun.*, 2023, **14**, 8466.

8 B. Zhang, S. Sun, Y. Jia, J. Dai, D. T. N. Rathnayake, X. Huang, J. Casasent, G. Adhikari, T. A. Billy, Y. Lu, X. C. Zeng and Y. Guo, *Adv. Mater.*, 2023, **35**, 2208336.

9 X. Xu, F.-T. Huang, K. Du and S.-W. Cheong, *Adv. Mater.*, 2022, **34**, 2206022.

10 S. Pandya, G. A. Velarde, R. Gao, A. S. Everhardt, J. D. Wilbur, R. Xu, J. T. Maher, J. C. Agar, C. Dames and L. W. Martin, *Adv. Mater.*, 2019, **31**, 1803312.

11 D. Yang, L. Luo, Y. Gao, S. Chen and X. C. Zeng, *Mater. Horiz.*, 2019, **6**, 1463–1473.

12 J. Cattermull, M. Pasta and A. L. Goodwin, *Mater. Horiz.*, 2021, **8**, 3178–3186.

13 D. Gonzalez-Cuadra, A. Bermudez, P. R. Grzybowski, M. Lewenstein and A. Dauphin, *Nat. Commun.*, 2019, **10**, 2694.

14 S. Wu, M. L. Klemm, J. Shah, E. T. Ritz, C. Duan, X. Teng, B. Gao, F. Ye, M. Matsuda, F. Li, X. Xu, M. Yi, T. Birol, P. Dai and G. Blumberg, *Phys. Rev. X*, 2024, **14**, 011043.

15 D. M. Lee, *Rev. Mod. Phys.*, 1997, **69**, 645–666.

16 P. Schlottmann, *J. Low Temp. Phys.*, 1975, **20**, 123–154.

17 S. S. Sharaya, B. A. Zakharov and E. V. Boldyreva, *Acta Crystallogr., Sect. B: Struct. Sci., Cryst. Eng. Mater.*, 2024, **80**, 94–104.

18 H. Kitatani, S. Miyashita and M. Suzuki, *J. Phys. Soc. Jpn.*, 1986, **55**, 865–876.

19 A. C. Anderson, W. Reese and J. C. Wheatley, *Phys. Rev.*, 1963, **130**, 1644–1653.

20 P. S. Pershan and J. Prost, *J. Phys., Lett.*, 1979, **40**, 27–30.

21 W. Nicolazzi and A. Bousseksou, *Cron. Chim.*, 2018, **21**, 1060–1074.

22 M. A. Halcrow, *Spin-crossover materials: properties and applications*, John Wiley & Sons, Ltd, Chichester, 2013.

23 J.-F. Dayen, N. Konstantinov, M. Palluel, N. Daro, B. Kundys, M. Soliman, G. Chastanet and B. Doudin, *Mater. Horiz.*, 2021, **8**, 2310–2315.

24 M. Piedrahita-Bello, J. E. Angulo-Cervera, A. Enriquez-Cabrera, G. Molnár, B. Tondu, L. Salmon and A. Bousseksou, *Mater. Horiz.*, 2021, **8**, 3055–3062.

25 E. Collet, G. Azzolina, J. Jeftić and M.-H. Lemée-Cailleau, *Adv. Phys.: X*, 2023, **8**, 2161936.

26 D. Chernyshov, H.-B. Bürgi, M. Hostettler and K. W. Törnroos, *Phys. Rev. B: Condens. Matter Mater. Phys.*, 2004, **70**, 094116.

27 M. Shatruk, H. Phan, B. A. Chrisostomo and A. Suleimenova, *Coord. Chem. Rev.*, 2015, **289–290**, 62–73.

28 N. Ortega-Villar, C. M. Muñoz and A. J. Real, *Magnetochemistry*, 2016, **2**, 16.

29 S. Ohkoshi, K. Imoto, Y. Tsunobuchi, S. Takano and H. Tokoro, *Nat. Chem.*, 2011, **3**, 564–569.

30 E. Pardo, C. Train, H. Liu, L.-M. Chamoreau, B. Dkhil, K. Boubekeur, F. Lloret, K. Nakatani, H. Tokoro, S. Ohkoshi and M. Verdaguer, *Angew. Chem.*, 2012, **124**, 8481–8485.

31 M. Hervé, G. Privault, E. Trzop, S. Akagi, Y. Watier, S. Zerdane, I. Chaban, R. G. Torres Ramírez, C. Mariette, A. Volte, M. Cammarata, M. Levantino, H. Tokoro, S. Ohkoshi and E. Collet, *Nat. Commun.*, 2024, **15**, 267.

32 V. B. Jakobsen, E. Trzop, E. Dobbelaar, L. C. Gavin, S. Chikara, X. Ding, M. Lee, K. Esien, H. Müller-Bunz, S. Felton, E. Collet, M. A. Carpenter, V. S. Zapf and G. G. Morgan, *J. Am. Chem. Soc.*, 2022, **144**, 195–211.

33 D. Paliwoda, L. Vendier, W. Nicolazzi, G. Molnár and A. Bousseksou, *Inorg. Chem.*, 2022, **61**, 15991–16002.

34 J.-F. Létard, P. Guionneau, E. Codjovi, O. Lavastre, G. Bravic, D. Chasseau and O. Kahn, *J. Am. Chem. Soc.*, 1997, **119**, 10861–10862.

35 M. J. Frisch, G. W. Trucks, H. B. Schlegel, G. E. Scuseria, M. A. Robb, J. R. Cheeseman, G. Scalmani, V. Barone, G. A. Petersson, H. Nakatsuji, X. Li, M. Caricato, A. Marenich, J. Bloino, B. G. Janesko, R. Gomperts, B. Mennucci, H. P. Hratchian, J. V. Ortiz, A. F. Izmaylov, J. L. Sonnenberg, D. Williams-Young, F. Ding, F. Lipparini, F. Egidi, J. Goings, B. Peng, A. Petrone, T. Henderson, D. Ranasinghe, V. G. Zakrzewski, J. Gao, N. Rega, G. Zheng, W. Liang, M. Hada, M. Ehara, K. Toyota, R. Fukuda, J. Hasegawa, M. Ishida, T. Nakajima, Y. Honda, O. Kitao, H. Nakai, T. Vreven, K. Throssell, J. A. Montgomery, Jr., J. E. Peralta, F. Ogliaro, M. Bearpark, J. J. Heyd, E. Brothers, K. N. Kudin, V. N. Staroverov, T. Keith, T. Kobayashi, J. Normand, K. Raghavachari, A. Rendell, J. C. Burant, S. S. Iyengar, J. Tomasi, M. Cossi, J. M. Millam, M. Klene, C. Adamo, R. Cammi, J. W. Ochterski, R. L. Martin, K. Morokuma, O. Farkas, J. B. Foresman, and D. J. Fox, *Gaussian 09*, Gaussian, Inc., Wallingford CT, 2016.

36 J. P. Perdew, K. Burke and M. Ernzerhof, *Phys. Rev. Lett.*, 1996, **77**, 3865–3868.

37 C. Adamo and V. Barone, *J. Chem. Phys.*, 1999, **110**, 6158–6170.

38 E. Tailleur, M. Marchivie, P. Negrier, D. Denux, S. Massip, D. Mondieig, G. Chastanet and P. Guionneau, *CrystEngComm*, 2019, **21**, 6246–6251.

39 D. Vladimir and P. Toledano, *Reconstructive Phase Transitions*, In Crystals and Quasicrystals, World Scientific, 1996.

40 M. A. Carpenter, E. K. H. Salje and A. Graeme-Barber, *Eur. J. Mineral.*, 1998, **10**, 621–691.

41 E. K. Salje, *Phase Transitions in Ferroelastic and Co-elastic Crystals*, Cambridge University Press, Cambridge, 1991.

42 V. Janovec, V. Dvořák and J. Petzelt, *Czech. J. Phys. B*, 1975, **25**, 1362–1396.

43 E. Collet and P. Guionneau, *Cron. Chim.*, 2018, **21**, 1133–1151.

44 G. Azzolina, R. Bertoni and E. Collet, *J. Appl. Phys.*, 2021, **129**, 085106.

45 Y. M. Gufan, *Phys. Solid State*, 1980, **22**, 951.

46 S. Iwagaki, H. Kakuta, Y. Yamamura, H. Saitoh, M. Hishida, K. Fukada and K. Saito, *Crystals*, 2020, **10**, 361.

47 S. P. Vallone, A. N. Tantillo, A. M. dos Santos, J. J. Molaison, R. Kulmaczewski, A. Chapoy, P. Ahmadi, M. A. Halcrow and K. G. Sandeman, *Adv. Mater.*, 2019, **31**, 1807334.

48 N. Brefuel, H. Watanabe, L. Toupet, J. Come, N. Matsumoto, E. Collet, K. Tanaka and J. P. Tuchagues, *Angew. Chem., Int. Ed.*, 2009, **48**, 9304–9307.

49 H. Watanabe, K. Tanaka, N. Bréfuel, H. Cailleau, J.-F. Létard, S. Ravy, P. Fertey, M. Nishino, S. Miyashita and E. Collet, *Phys. Rev. B*, 2016, **93**, 014419.

50 B. Kundys, M. Viret, D. Colson and D. O. Kundys, *Nat. Mater.*, 2010, **9**, 803–805.

51 N. A. Spaldin and R. Ramesh, *Nat. Mater.*, 2019, **18**, 203–212.

52 G. F. Nataf, M. Guennou, J. M. Gregg, D. Meier, J. Hlinka, E. K. H. Salje and J. Kreisel, *Nat. Rev. Phys.*, 2020, **2**, 634–648.

53 P. Tolédano and G. Li, *Phys. Rev. B*, 2021, **103**.